PHYSICAL REVIEW ACCELERATORS AND BEAMS **19,** 011301 (2016)

rf breakdown tests of mm-wave metallic accelerating structures

Massimo Dal Forno,[1,*] Valery Dolgashev,[1] Gordon Bowden,[1] Christine Clarke,[1]
Mark Hogan,[1] Doug McCormick,[1] Alexander Novokhatski,[1] Bruno Spataro,[2]
Stephen Weathersby,[1] and Sami G. Tantawi[1]

[1]*SLAC National Accelerator Laboratory, Menlo Park, California 94025, USA*
[2]*INFN/LNF Frascati, Via E. Fermi, 40, Frascati (Roma) 00044, Italy*

(Received 4 June 2015; published 6 January 2016)

We are exploring the physics and frequency-scaling of vacuum rf breakdowns at sub-THz frequencies. We present the experimental results of rf tests performed in metallic mm-wave accelerating structures. These experiments were carried out at the facility for advanced accelerator experimental tests (FACET) at the SLAC National Accelerator Laboratory. The rf fields were excited by the FACET ultrarelativistic electron beam. We compared the performances of metal structures made with copper and stainless steel. The rf frequency of the fundamental accelerating mode, propagating in the structures at the speed of light, varies from 115 to 140 GHz. The traveling wave structures are 0.1 m long and composed of 125 coupled cavities each. We determined the peak electric field and pulse length where the structures were not damaged by rf breakdowns. We calculated the electric and magnetic field correlated with the rf breakdowns using the FACET bunch parameters. The wakefields were calculated by a frequency domain method using periodic eigensolutions. Such a method takes into account wall losses and is applicable to a large variety of geometries. The maximum achieved accelerating gradient is 0.3 GV/m with a peak surface electric field of 1.5 GV/m and a pulse length of about 2.4 ns.

DOI: 10.1103/PhysRevAccelBeams.19.011301

I. INTRODUCTION

Accelerating gradient is one of the crucial parameters affecting the design, construction and cost of the next generation linear accelerators. The challenge is to develop reliable and cost-effective high-gradient accelerators.

The typical working frequencies of linear accelerators are from about 1 to 12 GHz. The accelerating gradient of the long-lived SLAC S-band linac is about 17 MV/m [1]. During development of the Next Linear Collider (NLC)/Global Linear Collider (GLC), an X-band test accelerator was built, which operated at 65 MV/m unloaded gradient [2,3]. The CERN based linear collider design CLIC requires 100 MV/m loaded gradient at 12 GHz in accelerating structures with heavy wakefield damping [4]. Future accelerators may need even higher gradients, such as compact synchrotron light sources or inverse Compton scattering gamma ray sources [5].

High gradient acceleration has several problems, of which rf breakdown, pulse heating and field emission are the major obstacles [6]. rf breakdowns limit the working power and produce irreversible surface damage in high power rf components and rf sources.

The work by Loew and Wang, published in 1988 [7], considered rf breakdowns directly linked to peak electric field. They were studying the peak limit value of the electric field that generates breakdowns. Their work was carried out at different frequencies: S-band, C-band, and X-band. They found that the maximum peak surface electric field achievable without rf breakdowns, grows with the square-root of the frequency. This analysis led to the idea that maximum accelerating gradient, limited by breakdown, increases with frequency. Later, other research carried out at CERN [8] in the frequency range from 21 to 39 GHz, concluded that there is no increase in the maximum achievable gradient at higher frequencies. Both studies considered breakdown as a phenomenon generated when the peak electric field exceeds a certain threshold.

Other studies to understand and mitigate the effects of rf breakdown were conducted during the development of the normal-conducting 11.424 GHz NLC/GLC [2,3,9], which has been replaced by the 12 GHz CERN-based linear collider CLIC [10]. Advances in understanding limitations on accelerating gradient go beyond linear colliders. Accelerators are used in applications such as inverse Compton scattering gamma ray sources [5], compact free-electron lasers (FELs) [11,12], and compact medical linacs for hadron therapy [13]. Modern high gradient devices such as photo-rf guns [14], 4th harmonic linearizers for FELs [15], rf deflectors [16,17], and rf undulators [18,19], all use these technologies and methods,

---

[*] dalforno@slac.stanford.edu

TABLE I. Symbols and abbreviations used in this papers.

c	Speed of light
d	Cell length period
$\Delta\phi$	Phase advance
k_z	Propagation constant $(= \omega_0/c)$
R_s	Shunt impedance per unit length
P_d	Dissipated power in one cell
U	Stored energy in one cell
P	Power flow through the cavity cross-section
κ	Loss factor per unit length
v_g	Group velocity
t_p	Pulse length
l_{att}	Attenuation length
V	Integrated accelerating voltage
E_z	Longitudinal electric field
Q_0	Unloaded quality factor
q	Bunch charge
σ_z	Bunch length
L	Total length of the structure
a	Half gap

developed and sustained by studies of high gradient accelerators.

During the NLC/GLC work the statistical nature of rf breakdown became apparent [2,3,9,20]. For most accelerating structures exposed to the same rf power and pulse shape, the number of rf breakdowns per pulse is nearly steady or slowly decreasing over $10^5 - 10^7$ pulses. The breakdown probability became one of the main quantitative requirements characterizing high gradient performance of linacs. For example: the CLIC linear collider requires rf breakdown probability to be less than 4×10^{-7} per pulse per meter for a loaded accelerating gradient of 100 MV/m.

As technology progressed, sophisticated manufacturing and surface preparation techniques and systematic rf processing methods were developed [21–23]. As a result of this R&D, practical 11.4 GHz traveling wave (TW) accelerating structures, which are CLIC prototypes, run at breakdown rates of about 10^{-6} per pulse per meter at unloaded gradients up to 120 MV/m and ~200 ns pulse length. TW structures that include wakefield damping work at about 100 MV/m for similar breakdown rates [24]. Studies of new geometries and materials at 11.424 GHz show the potential to reach 150 MV/m accelerating gradients with similarly low breakdown rates [25].

Presently, X-band structures are the most studied in terms of rf breakdowns [20,26–29]. We know that breakdown statistics depend on pulse heating [30] and a numerous list of other factors, such as the peak electric field, the peak magnetic field [31], and the peak Poynting vector [32]. In this paper, using all the knowledge and technologies developed in designing, fabricating, and testing for X-band structures, we want to explore the physics of rf breakdowns at mm-wave frequencies.

W-band metallic and dielectric structures were previously studied at SLAC by Whittum *et al.* [6,33–37]. Also Hill *et al.* [38–41] tested both a single metallic W-band cavity and a dielectric linear accelerator excited with an electron beam. They studied the longitudinal and transverse wakefields in a 91 GHz dielectric coated accelerating structure [42]. Henke and Bruns [43–46] and Chou and Kroll at SLAC designed a W-band muffin-tin planar accelerator structure [47–49]. These studies highlight the difficulties of working at W-band frequencies. The challenge was to accurately assemble the structure from its parts [50].

Another approach to reaching high accelerating gradients at higher frequencies involves dielectric wakefield accelerators. These schemes have been tested at SLAC FACET [51] and elsewhere [52–55]. To our knowledge, in these experiments there were no systematic studies of rf breakdown probability. In our metallic structures we can detect the breakdowns by using a new diagnostic tool that we called “arc detector,” unique to our structures.

We built a high gradient linear accelerating structure, traveling wave with constant impedance. The structure is open, consists of two separate halves. To reduce field enhancement all edges were rounded. The advantage of an open structure is that there is less risk in manufacturing and testing than for a clamped or brazed structure. Moreover, with the open structure we were able to vary the gap between the two plates, changing the rf parameters. We also changed the gradient by changing the relative position of the beam with respect to the center of the structure. The two halves can be independently insulated from each other and ground. These insulated metal halves constitute the arc detector, used to measure the field emission current and detect breakdowns. Its implementation is described in the next chapter.

In this paper we show the results of studies on rf breakdowns performed with mm-wave accelerating structures. Since we do not have access to mm-wave rf generators, the structure needs to be excited by an ultrarelativistic electron beam.

With X-band accelerating structures we tested cavities of many different types, testing several cavities of each type [20,22,23,26,27]. To confirm reproducibility of experimental data, several cavities of the same type were tested. Testing of each X-band structure took many weeks or months. The same procedure is impossible to repeat at FACET, where each experiment lasts an 8–10 h shift with weeks in-between. Therefore, we used an approach different from our X-band work, we tried to explore as much parameter space as possible: standing wave vs. traveling wave, copper vs. stainless steel. We plan to continue expanding this parameter space in new experiments.

This paper is divided into four sections. In the first section we present the design considerations and the geometries of the structures. In the second section we present the method that we developed to estimate the wakefield induced by the beam. The third section presents the numerical results of gradients and peak fields. In the fourth section we present the experimental results. In the third experiment we designed a new method to detect breakdowns and field emission current. We used the scanning electron microscope (SEM) inspection to determine the nondamage conditions.

All symbols used in this paper are presented in Table I.

II. DESIGN CONSIDERATIONS AND GEOMETRY OF THE STRUCTURES

In our experiments we studied breakdowns in mm-wave structures. Since we do not have access to mm-wave rf sources, we designed wakefield-excited structures. The beam was generated by FACET [51], housed in the first 2 km of the SLAC linear accelerator [1]. FACET has an energy of 20.35 GeV, and about 50 μm of longitudinal bunch length. The charge varies from 2.7 to 3.2 nC. The structures are open type, composed of two separate movable metal halves. The horizontal position, the vertical position and the gap are remotely controlled by three movers. The cavities are milled into the flat side of metal blocks. When the two halves are placed together they form a single accelerating structure. Each cell has been designed with a mode close to $2\pi/3$ phase advance. The edges have been rounded to minimize the peak fields. The field of the fundamental accelerating mode is trapped inside when the gap is less than 1.3 mm. The rf parameters can be changed by varying the gap. Both input and output couplers are symmetric dual-feed, radiating energy out through antenna horns to pyrodetectors. The electromagnetic design was carried out with Ansys HFSS [56].

Three types of structures have been designed and tested. The first is a copper traveling wave structure, operating in the standing wave regime (in this paper we will call it "SW") [Fig. 1(a)], the second is a copper traveling wave structure and the third is a stainless steel traveling wave structure [Fig. 1(b)], at the bottom-left and top-right, respectively. The solid model of the geometry of the second and third structure is shown in Fig. 2(a), while a photo of the structure, including the near coupler cells, the output coupler, and the horns is shown in Fig. 2(b). In the zero gap condition, there is no path for the beam to travel, as the two blocks are in contact with each other.

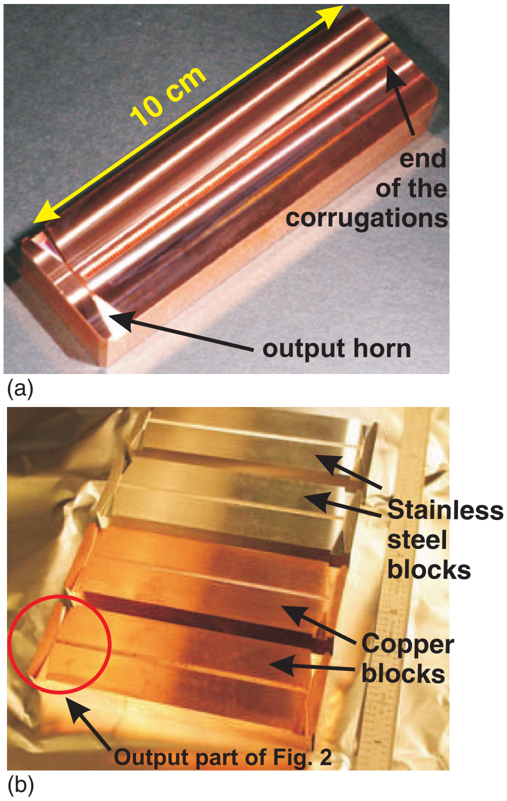

FIG. 1. Picture of the mm-wave traveling wave copper structure operating in the standing wave regime (a), and of the traveling wave copper and stainless steel structures, at the bottom-left and top-right, respectively (b).

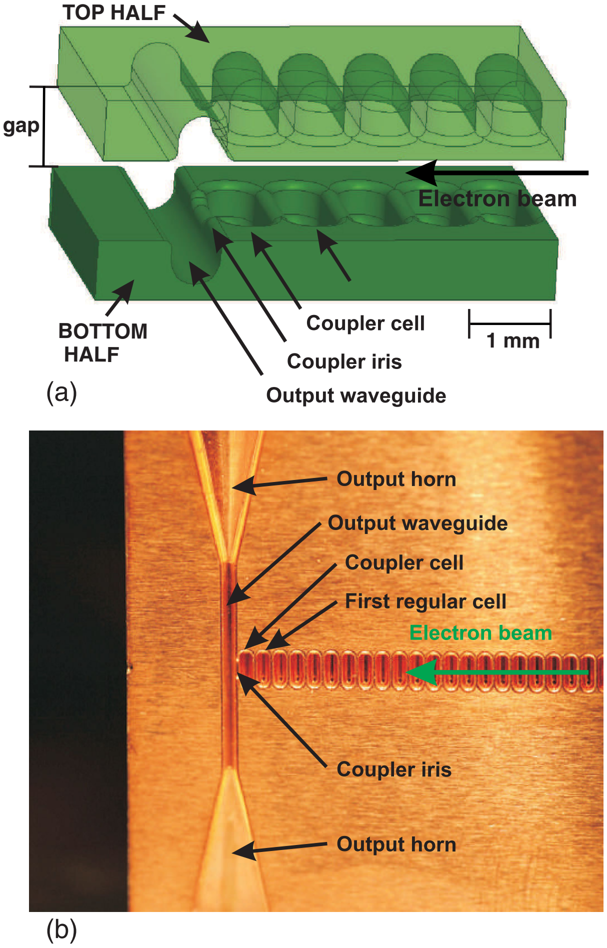

FIG. 2. The mm-wave traveling wave accelerating structure with detail of the output part, including coupler and output waveguides. Solid model (a) and picture (b).

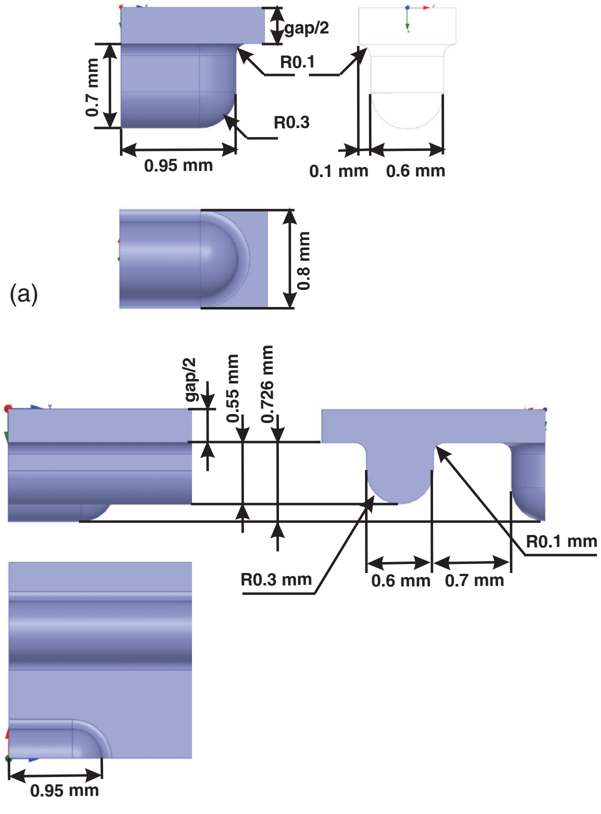

FIG. 3. Geometry of one quarter of the vacuum part (simulated by Ansys HFSS) of the regular cell (a) and of the coupler of the SW structure (b).

The two blocks of the first structure were machined by Makino [57] in May 2012, while the two blocks of the second and third structures were produced by EDM Department Inc. [58]. The profile roughness parameter Ra is 0.2–0.3 μm. The halves were cleaned according to the SLAC procedure established for X-band high gradient structures [21–23].

In the first experiment we used the copper traveling wave structure, operating in the standing wave regime. It has an undercoupled coupler of about −30 dB, because we wanted to separate the effects of the external environment (reflections by mirrors, windows and other surrounding objects) from our studies of rf breakdowns inside the structure. As depicted in Fig. 1(a), the corrugations end with a short-circuit on the right end, and with undercoupled coupler-horns on the left end.

In the first experiment we did not have gap motors and the gap was fixed at 0.9 mm. The geometry of the vacuum part of the first experiment regular cell is shown in Fig. 3(a), while the coupler is in Fig. 3(b).

Since the coupler is undercoupled it radiates a low output power. In the first experiment we found that the useful rf detected signal is low compared to the ambient electromagnetic noise. Therefore we decided to increase the coupling in the following experiments. In the second experiment we used the copper traveling wave structure and in third experiments we used the stainless steel traveling wave structure, both with matched couplers. The matching procedure is described in [59,60]. The geometry of the vacuum part of the TW regular cell is shown in Fig. 4(a), while the coupler is in Fig. 4(b).

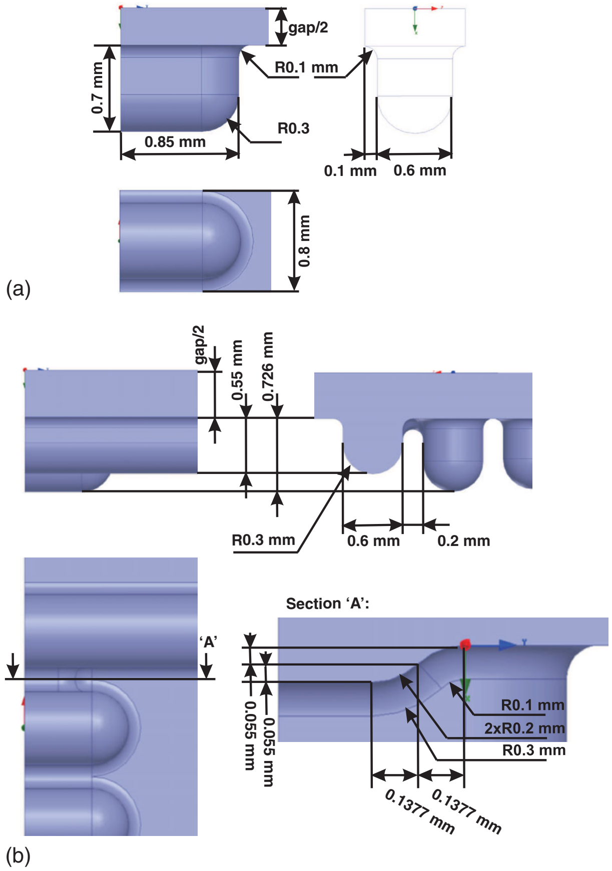

FIG. 4. Geometry of one quarter of the vacuum part (simulated by HFSS) of the regular cell (a) and of the coupler of the TW structure (b).

For each experiment we recorded the pyrodetector or the crystal-detector voltage, which is proportional to the pulse energy emitted from the output waveguide horn from the structure. In the first two experiments we did not see any signatures of rf breakdowns on the output signals. Thus we had to invent a new diagnostic able to reliably detect breakdowns. Since breakdowns generate electron and ion currents, we decided to build an arc detector unique to open structures. In the third experiment the two metal halves were electrically insulated. We measured the field emission current and the breakdown current by measuring the voltage induced between the structure blocks. This was achieved by connecting the two metal halves to an oscilloscope. We can clearly see voltage spikes correlated with the transverse position of the electron beam inside the cavity and the magnitude of the pyrodetector signal.

We assumed that these voltage spikes are due to currents generated by rf breakdowns.

III. WAKEFIELD COMPUTATION

The electromagnetic fields in the structure are excited by the FACET electron beam. We are interested in calculating the long range wakefield and the accelerating gradient induced by this bunch. A wakefields calculation method has been developed using HFSS and MATHEMATICA [61], operating in the frequency domain. This method calculates the rf parameters of periodic eigensolutions. This method underestimates the short-range wakefield, since we focused on trapped modes. These computations take into account the wall losses and are applicable to complex cell geometries. With this wakefield computational tool it is possible to calculate the longitudinal wakefunctions, the accelerating gradient induced in the structure, the surface peak field and the power radiated from the waveguide. It is also possible to distinguish the accelerating gradient of the fundamental mode and the total gradient generated by the trapped modes.

The assumption in our calculations is that the structure is periodic and that the electron beam is traveling at the speed of light. Considering a regular cell, the synchronous frequency is the frequency at which the phase velocity of the traveling wave is equal to the beam velocity. Therefore the synchronous frequency is the frequency of the wave induced by the beam.

The synchronous frequency, and phase, falls at the intersection between the cell dispersion curve and the speed of light. The dispersion curve of the cell has been evaluated by modeling the regular cell in HFSS, and running the eigenmode simulations using HFSS "master-slave" boundaries [56] (applied as depicted in Fig. 5). The "master" and the "slave" boundaries allow us to simulate the field distributions of an infinite periodic cell array, by simulating only one cell. By setting a $\Delta\phi$ phase advance between the "master" and the "slave" planes, an eigenmode solution is calculated, which is equivalent to the field traveling in an infinite periodic array of cells at the simulation frequency. To improve the simulation speed, only a quarter cell has been analyzed by setting magnetic symmetry planes in "XZ" and "YZ" (see Fig. 5). With this setting the dipole mode is excluded from our simulations, since we are only interested in the accelerating one.

A "master-slave" $\Delta\phi$ phase parametric sweep was simulated from 0 to 180 degrees with a step size of 5 degrees, recording at each step the simulated resonant frequency. The dispersion curve was obtained by interpolating the simulated points. The line representing the speed of light is given by the relation: $f = \frac{c}{360d}\Delta\phi$, and the synchronous frequency and phase are given by the intersection of the two curves. An example of such an intersection, for the fundamental mode, is shown in Fig. 6. The derivative of the dispersion curve is positive, therefore the power flow is in the same direction of the beam and it is a "forward" type mode.

The rf parameters were calculated simulating the regular cell by setting the "master-slave" boundaries with the phase delay corresponding to the synchronous phase advance (which generates the synchronous frequency) and by using the following relations. The accelerating voltage is given by:

$$V = \int_0^d E_z e^{\pm i k_z z} dz. \tag{1}$$

The "±" integration sign is chosen for forward (+) or backward (−) wave.

The shunt impedance (per unit length):

$$R_s = \frac{V^2}{P_d}\frac{1}{d}. \tag{2}$$

The loss factor (per unit length) including the group velocity related compression factor [62–64]:

$$\kappa = \frac{V^2}{4U}\frac{1}{d}\frac{1}{1 - v_g/c}. \tag{3}$$

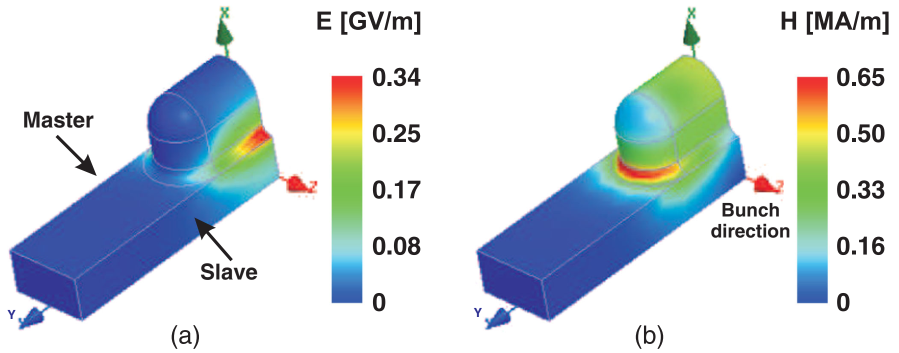

FIG. 5. Plot of the electric field (a) and of the magnetic field (b) of the eigenmode solutions of one quarter of period of the first copper cell (gap = 0.9 mm), at the synchronous frequency. Considering an infinite traveling wave structure these fields are excited by a bunch of charge of 2.7 nC and 50 μm long.

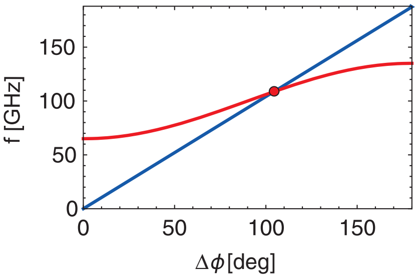

FIG. 6. Dispersion curve (red) and speed of light line (blue), with intersection at the synchronous point (for clarity we show a very high group velocity structure).

The group velocity:

$$v_g = P/(U/d). \tag{4}$$

The attenuation length:

$$l_{\mathrm{att}} = \frac{P}{P_d} d\left(1 - \frac{v_g}{c}\right) = v_g \frac{Q_0}{\omega_0}\left(1 - \frac{v_g}{c}\right). \tag{5}$$

The pulse length of a structure of length L, assuming the attenuation length is significantly longer than 'L':

$$t_p = \frac{L}{v_g}\left(1 - \frac{v_g}{c}\right). \tag{6}$$

After calculating the above rf parameters from the eigenmode data, the following expressions are the quantities induced by the beam, for a given mode:

The induced accelerating gradient:

$$E_{z0} = 2\kappa q \exp\left(-\frac{\omega_0^2 \sigma_z^2}{2c^2}\right). \tag{7}$$

The induced power flow:

$$P = \kappa q^2 v_g \frac{1}{1 - v_g/c} \exp\left(-\frac{\omega_0^2 \sigma_z^2}{c^2}\right). \tag{8}$$

The pulse energy:

$$U_p = \int_0^{t_p} P \exp\left(-\frac{v_g t}{l_{\mathrm{att}}}\right) dt = P \frac{l_{\mathrm{att}}}{v_g}\left[1 - \exp\left(-\frac{v_g t_p}{l_{\mathrm{att}}}\right)\right]. \tag{9}$$

A. Calculation of higher order mode rf parameters

The rf parameters for the higher order modes that exist in the structure are crucial to obtain the total wake potential. The trapped wake is the sum of all the generated wakes with frequencies below the beampipe cutoff. The above procedure has been used to calculate the synchronous frequencies and phases of the high order modes with some precautions. Depending on the bunch interaction between the forward or backward wave, it is important to determine the sign of the integration of Eq. (1).

The eigenmode "master-slave" simulation was carried out for each mode, but at higher frequencies the modes have phase advances per cell larger than 180 degrees. The analysis should be completed with a phase extended version of the dispersion diagram, called an "unfolded" version [an example is shown in Fig. 7(a)], where the phase advance is not limited to 0–180 degrees. In Fig. 7(a) both modes are "forward" type, because at the intersections, both dispersion curves have positive derivatives. To reduce the simulation time, we restrict the phase diagram to 0–180 degrees, folding in the speed of light line, generating the "folded" dispersion diagram [an example is shown in Fig. 7(b)]. In the latter diagram it is important to determine whether the high order modes are "forward" or "backward". The green line is "forward" because, even though it has a negative derivative, it is intersecting with a speed of light line folded once (odd vs. even). To avoid errors in determining if the mode is "forward" or "backward," we developed a robust method to calculate the shunt impedance with the correct integration sign. The shunt impedances plus and minus (R_{s+} and R_{s-}) correspond to the forward and backward wave, calculated by setting plus or minus sign on Eq. (1). After making the eigenmode simulation of one cell, we longitudinally replicated the on-axis fields. One of the two integrated impedances (R_{s+} or R_{s-}) grows while the other trends toward zero. The shunt impedance that is linearly growing is the one interacting with the electromagnetic field. We tested this method in a noncorrugated waveguide (no interaction with beam), which showed that both R_{s+} and R_{s-} tend toward zero when longitudinally repeating the cell fields.

We calculated the shunt impedances and loss factors induced in the periodic structure. For each trapped higher-order mode, this procedure was used to calculate the loss factor that interacts with the beam. Summing all the trapped modes, the Green's function (also called the wakefunction) is given by:

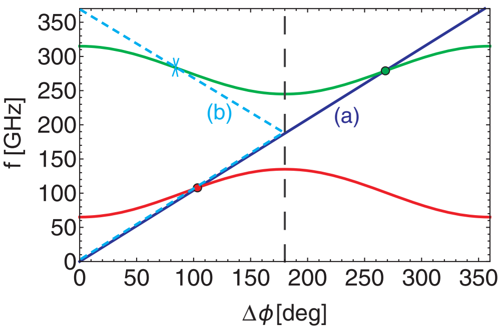

FIG. 7. Plot (a): Unfolded dispersion curve of the first and second mode (red and green) and speed of light line (blue), with intersection at the synchronous points. Plot (b): Folded dispersion curve of the first and second mode (red and green) and folded speed of light line (cyan-dashed), with opposite intersection for the high order mode.

TABLE II. rf parameters of the first copper structure, with 0.9 mm gap and 1 nC bunch.

gap [mm]	f [GHz]	$\Delta\phi$ [deg]	Q_0	R_s [$M\Omega$/m]	κ [MV/(nC m)]	v_g [%]	t_p [ns]	l_{att} [mm]	P [MW]	E_{z0} [GV/m]	E_{max} [GV/m]	H_{max} [MA/m]
0.9	115.66	111.12	2041	180	18	12.4	2.45	91	0.758	0.034	0.13	0.24

$$g(t) = u(t)\sum_{i=1}^{N} 2\kappa_i \cos(\omega_i t) \tag{10}$$

where $u(t)$ is the unitary step function and "N" is the number of trapped modes. The wakepotential is obtained by convolving the cosine-step function term of the previous expression with the bunch charge distribution. Considering a Gaussian bunch, the final expression is

$$w(t) = \sum_{i=1}^{N} 2\kappa_i \int_{-\infty}^{t} \frac{1}{\sqrt{2\pi}\sigma_t} \exp\left(-\frac{1}{2}\frac{\tau^2}{\sigma_t^2}\right) \cos(\omega_i(t-\tau))d\tau. \tag{11}$$

Our method has been verified by comparing the results with another wakefield calculation method developed by Novokhatski [65–68], showing good agreement.

IV. NUMERICAL RESULTS

In this section we show the numerical results obtained by applying the method above described to the three structures.

A. Traveling wave copper structure, operating in the standing wave regime

The first experiment involved a traveling wave copper structure, operating in the standing wave regime. When the bunch excites the field, the field is reflected at the coupler and creates a standing wave pattern. In this experiment we did not have a gap mover. The gap between the two metal halves was fixed at 0.9 mm. The geometry of the vacuum part (modeled in HFSS) of the regular cell is shown in Fig. 3(a), while the coupler is in Fig. 3(b). The rf parameters calculated with the above method are listed in Table II. The fundamental mode is dominant, all the other modes are above cutoff and therefore are not trapped in the structure.

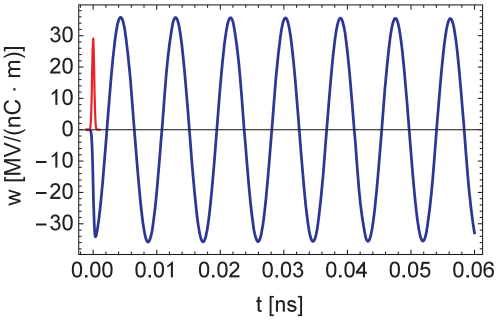

FIG. 8. Wakefield of the only trapped mode (blue), electron bunch shape (red), for the first copper structure, with gap = 0.9 mm.

The wakefield has been calculated using Eq. (11), and is shown in Fig. 8 over a short range. This wakefield, multiplied by the bunch charge gives the accelerating gradient.

A simulation of the power generated by the bunch is depicted in Fig. 9. The energy of this pulse is 7.4 mJ with 2.7 nC bunch.

The peak electric and magnetic fields are shown in Fig. 5, for the 2.7 nC bunch charge used in the first experiment.

B. Traveling wave copper and stainless steel structure

The second and third experiments involved a traveling wave structure. We needed a matched coupler in order to have large signal to noise ratio. Both structures are installed with a remotely controlled motor for adjusting the gap. The gap can be remotely changed from 0 mm to about 40 mm. The gap range used in the experiments is from 0.2 to 0.9 mm. The structures were made with copper (for the second experiment) and stainless steel (for the third experiment). They are depicted in Fig. 1(b). The geometry of the vacuum part (simulated by HFSS) of the regular cell is shown in Fig. 4(a), while the coupler is in Fig. 4(b).

1. Coupler matching

During the last two experiments we tested the structures with different gaps. The coupler can only be matched for a fixed gap. Thus when we match the coupler we must choose a good trade-off that allows reasonable transmission when changing the gap afterwards. In this exercise we used a gap range from 0.3 to 0.9 mm. Figure 10 shows the reflection and the transmission when the coupler is matched for a certain gap, and the gap is changed afterwards. Figure 10(b) shows that if the coupler is matched at

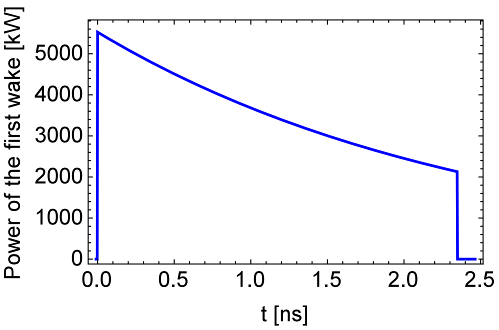

FIG. 9. Pulse of the power induced by the 2.7 nC bunch.

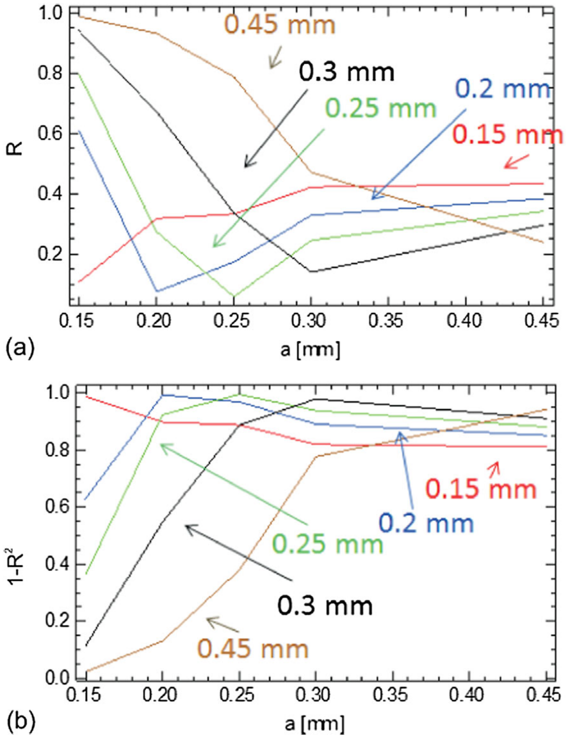

FIG. 10. Coupler reflection (a) and transmission (b), as a function of the gap aperture, for couplers matched for specific apertures ($a = 0.15$, 0.2, 0.25, 0.3, 0.45 mm). These plots show that matching the coupler to $a = 0.15$ mm does not produce significant mismatches when the gap is changed, where "a" is the half gap.

$a = 0.15$ mm, the transmission will not be affected by more than 20% by changing the gap. Therefore, for the final design, we used the coupler matched at $a = 0.15$ mm. Figure 2 is a picture of the manufactured structure.

2. Numerical results of the traveling wave structures

The rf parameters were calculated for gaps equal to 0.2, 0.3, 0.5, 0.7, 0.9 mm. For the fundamental mode the rf parameters are listed in Table III.

We were not able to use gap smaller than 0.2 mm because at smaller gaps the beam hits the structure. For the 0.2 mm gap, the attenuation length is only a couple of cells in the copper structure case. In this case the assumption that the power lost in the cavity wall is negligible with respect to the Poynting power flow, is no longer valid. Therefore the calculated group velocity is an approximation, as for the stainless steel case.

All the trapped modes must be considered to calculate the integrated loss factor, shown in Fig. 11, for different gaps. For each gap we calculated the wakefield, the power radiated from the output waveguide, and the fields.

With a gap of 0.3 mm the coupler is matched. For the other gaps the power of the fundamental mode exiting from the waveguide is calculated by taking into account the transmission: $P_{\mathrm{out}} = P(1 - |R|^2)$. The output signals collected outside of the waveguide are depicted in Fig. 12, for the copper structure (a) and for the stainless steel structure (b). Figure 13 is a series of plots that describe the results of the simulations for the second and third traveling wave structures.

Figure 13(a) shows the synchronous frequency; Fig. 13(b) the decay length; Fig. 13(c) the group velocity; Fig. 13(d) the peak and accelerating electric field.

To analyze the origins of breakdowns, we are interested in the peak electric and the magnetic fields on the copper surface, considering the highest gradient that was achieved with the smallest gap (0.2 mm). Such fields are derived from an HFSS simulation of the fundamental mode, excited by 3.2 nC of bunch charge (charge used in the second experiment, TW copper). They are shown in Fig. 14.

The wakefield of the first mode and the sum of all the wakes have been calculated using Eq. (11). The wakefields of the trapped modes for each gap are shown in Fig. 15. Figure 15(d) corresponds to the maximum gap. Here only one mode is trapped.

During the experiments, the beam axis was fixed and the structure was moved along the horizontal "Y" dimension (The coordinate system is the same as in Fig. 5.). When the electron beam passes over the corrugations of the structure, the wakefield changes. Figure 16 shows the accelerating gradient (a), output power (b), copper pulse energy (c), stainless steel pulse energy (d), as a function of the transverse position of a 3 nC electron beam (used in the third experiment, TW steel), for different gaps. Note that for easy comparison we used the 3.2 nC charge used in the second experiment for all the graphs. Plots (b)–(d) take into account the coupler reflection.

TABLE III. rf parameters of the TW copper (C) and stainless steel (S) structures, for the fundamental mode, with 1 nC bunch.

gap [mm]	f [GHz]	$\Delta\phi$ [deg]	$Q_0(C)$	$Q_0(S)$	$R_s(C)$ [$M\Omega$/m]	$R_s(S)$ [$M\Omega$/m]	κ [MV/(nC m)]	v_g [%]	$l_{\mathrm{att}}(C)$ [mm]	$l_{\mathrm{att}}(S)$ [mm]	P [MW]	E_{z0} [GV/m]	E_{max} [GV/m]	H_{max} [MA/m]
0.2	140.28	134.8	2070	286	449	62	47.45	0.21	1.5	0.2	0.03	0.095	0.2	0.4
0.3	136.27	130.9	2045	282	398	54	41.60	0.85	6.0	0.8	0. 105	0.083	0.19	0.356
0.5	130.30	125.2	2012	277	298	41	31.15	3.54	25.2	3.5	0.34	0.0625	0.174	0.347
0.7	126.01	121.0	2012	277	222	30	23.50	7.65	53.8	7.4	0.58	0.047	0.16	0.344
0.9	122.66	117.9	2037	281	166	23	17.87	12.4	86.2	11.9	0.754	0.0356	0.15	0.3

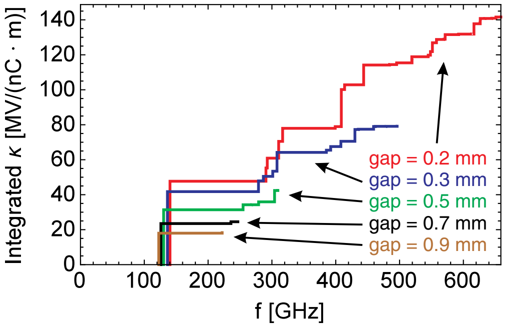

FIG. 11. Integrated loss factors for the TW structure, for all the analyzed gaps.

V. EXPERIMENTAL RESULTS

In this section we show the experimental results carried out using the three accelerating structures. For each experiment we describe a common procedure.

The electron beam has an energy of 20.35 GeV and a longitudinal bunch length of 50 μm.

A. Common procedure

The common procedure is divided in three main stages: operations before beam, operation with beam, and inspections after beam exposure.

The common operations before beam are (i) Machining: The first structure was manufactured by the company Makino [57], while the second and the third was manufactured by EDM Department Inc. [58]. (ii) Cleaning: The structures are cleaned according to SLAC procedure developed for the high-gradient X-band program. (iii) Installation: The structure is installed on motorized stages. In the first experiment we had control of the horizontal and vertical position, while in the second and third experiments we also controlled the gap. The assembly is then installed in the “Kraken” vacuum chamber. A mirror is glued to the structure for laser alignment, and a phosphor screen is bolted to the edge of the structure to visualize the electron beam. The antenna horns of the structure are directed toward pyrodetectors that sense the pulse energy. (iv) Alignment with the laser: A laser beam is placed on the trajectory of the FACET electron beam from the previous run. We moved the structure until the laser beam hit the mirror and then started the alignment procedure by tilting the structure with pitch screws. The structure is considered aligned when the reflected laser beam travels back along the same trajectory as the forward laser beam. (v) Pumping: The Kraken chamber is closed to establish vacuum.

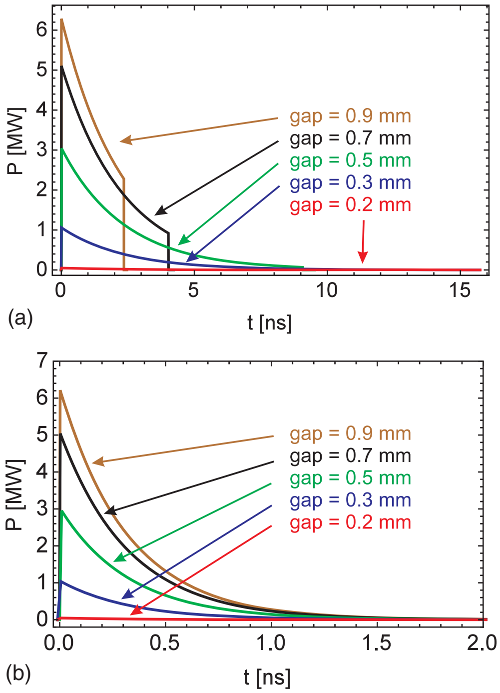

FIG. 12. Output power signals from the waveguide generated by a 3.2 nC bunch of 50 μm, taking into account the reflection at the coupler, for the copper structure (a) and the stainless steel structure (b).

Operations with the electron beam are the following: (i) Detect the beam on the phosphor screen: If the electron beam hits the copper structure, it will cause damages to the delicate part of the corrugations. Therefore, as a first step, we must steer the beam onto the phosphor screen, which is installed far from the corrugations. (ii) Finding the vertical center of the structure: When the gap is set, we must find the vertical position of the structure that allows the beam to be vertically centered. This is done by setting the electron beam at an approximate vertical center (horizontally it is far from the corrugations). The structure is slowly moved up (and down), till the beam slightly touches the copper, generating a radiation shower, detected by the accelerator control system. The vertical center is calculated taking the average between these upper and lower limits. (iii) Horizontal scan: Once we determined the vertical center, the structure is moved horizontally, letting the beam interact with the corrugations, generating the electromagnetic field. During each scan, we observed the magnitude of the energy pulses produced by the structure with pyrodetectors. In the third experiment we also observed the field emission current and detected breakdowns using the “arc detector” setup. (iv) The scan procedure is then repeated with different gaps (second and third experiment).

The after-beam operations are (i) The structure is removed and brought to the laboratory for inspection. (ii) The structure is inspected with SEM, looking for signs of damage due to rf breakdowns. The position of each damage is then noted. (iii) Considerations and speculations: We correlate the numerical calculated magnitude of the electric field with damage. From this comparison we can determine the peak electric field and pulse length at which the structures were not damaged by rf breakdowns.

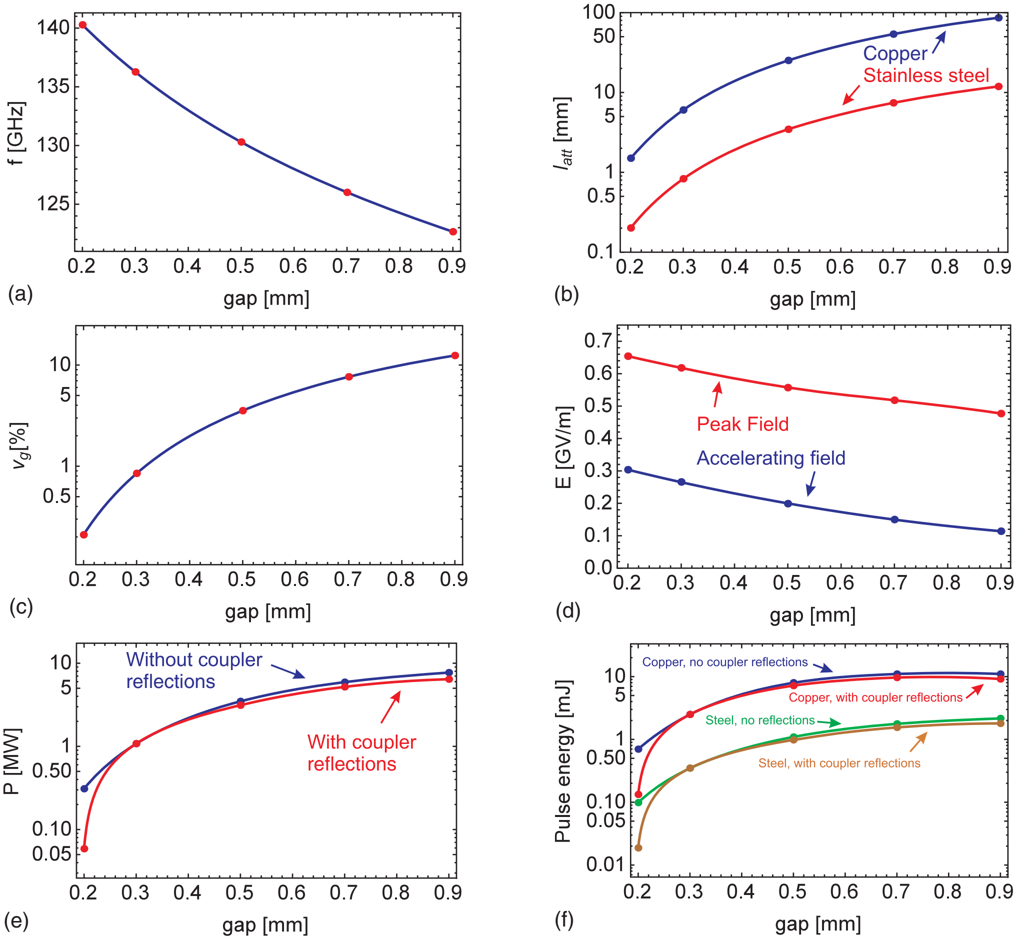

FIG. 13. Synchronous frequency (a), decay length (b), group velocity (c), peak and accelerating electric field (d), peak power traveling along the cells, and power exiting from the waveguide considering the reflection (e), pulse energy with and without considering the coupler reflection (f) with respect to the gap, for 3.2 nC and 50 μm long bunch.

Our FACET tests were done in a large vacuum chamber, which is used by many different experiments, thus it is opened and closed every week. In the first experiment (copper TW structure, operating in the standing wave regime) the average pressure was 9.6×10^{-7} Torr. In the second experiment (copper TW structure) it was 5.8×10^{-7} Torr, and in the third experiment (stainless steel TW structure) it was 3×10^{-7} Torr. This setup makes it impossible to reach vacuum pressures comparable with our X-band high gradient structures. We are aware of this problem and decided to proceed with the experiments anyway, since there is no data available in the studied parameter space.

As the study progressed, in each new experiment we improved the control system and diagnostics. Details of each experiment are described as follows.

B. First experiment: Traveling wave copper structure operating in the standing wave regime

We assembled the two halves of the accelerating structure with a fixed full gap of 0.9 mm. The structure was

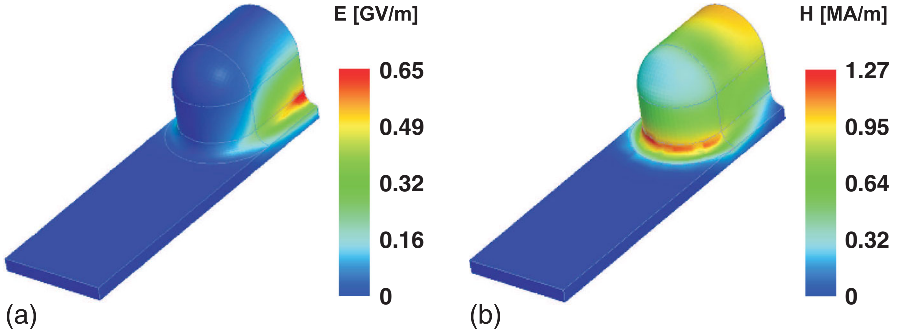

FIG. 14. Plot of the electric field (a) and of the magnetic field (b) of the eigenmode solutions of one quarter of period of the TW cell (gap = 0.2 mm), at the synchronous frequency. Considering an infinite traveling wave structure these fields are excited by a bunch of charge of 3.2 nC and 50 μm long.

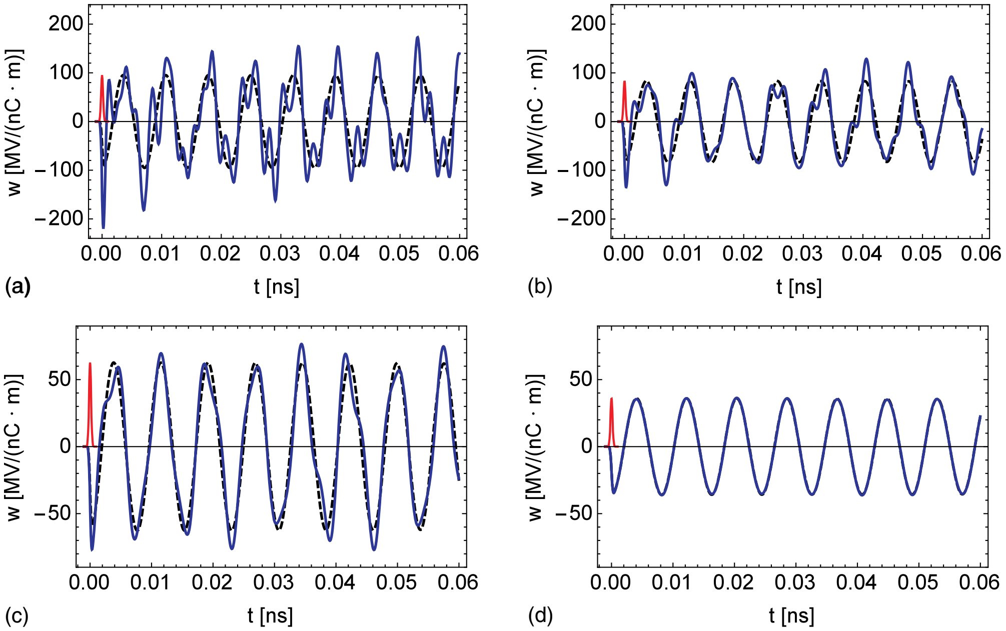

FIG. 15. Wakefield of the first mode (black dashed), total wakefield (blue), electron bunch shape (red), of the TW copper structure, for 0.2 mm gap (a), for 0.3 mm gap (b), for 0.5 mm gap (c), for 0.9 mm gap (d).

installed into the "Kraken" vacuum chamber (Fig. 17). It was aligned to the beam trajectory using the reference laser. This alignment allows the electron beam to pass cleanly through the gap between the top and bottom halves of the structure. Motorized stages are used to shift the structure horizontally or vertically with respect to the electron beam.

During the first experiment, the structure was exposed to the electron beam with 2.7 nC of bunch charge. The structure has been moved along the horizontal direction. At first, the beam crossed the structure where the corrugations are not present. By moving the structure along the horizontal direction, the corrugations intercepted the field of the electron beam, generating a power flux and an accelerating gradient. The maximum gradient occurred when the beam is on the structure axis (Fig. 17). When the beam is moved further from corrugations the gradient decreases.

After the experiment, we inspected the structure surfaces with a SEM microscope. The SEM inspection shows the location of damage due to rf breakdowns (Fig. 18). The first regular cell that is close to the coupler was damaged the

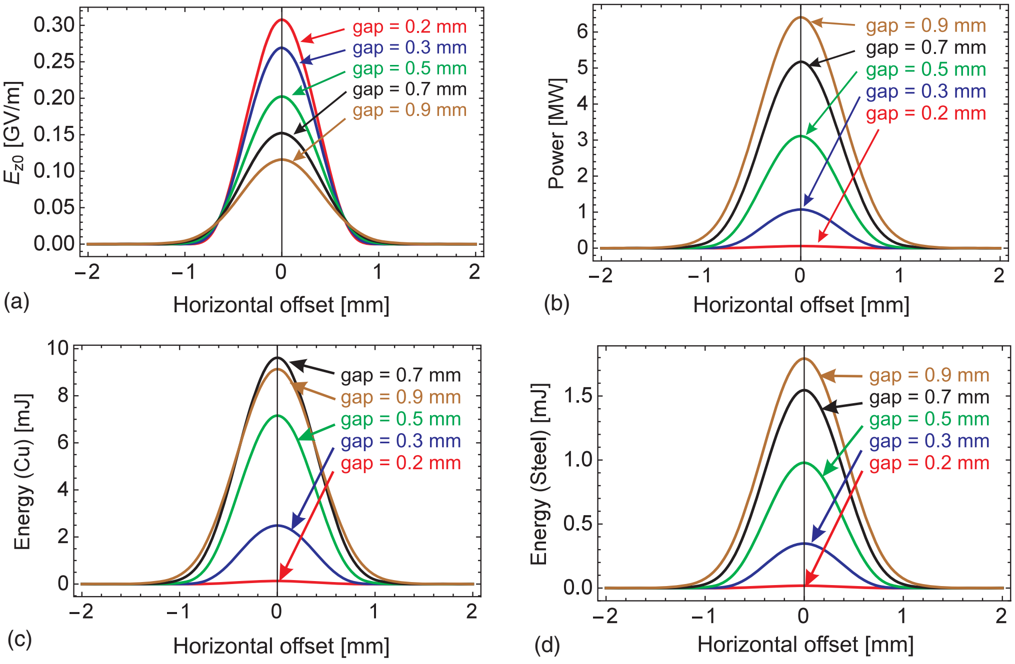

FIG. 16. Accelerating gradient (a), output power (b), copper pulse energy (c), stainless steel pulse energy (d), in function of the position of a 3.2 nC electron beam relative to the center of the corrugations. Plots (b)–(d) take into account the coupler reflection.

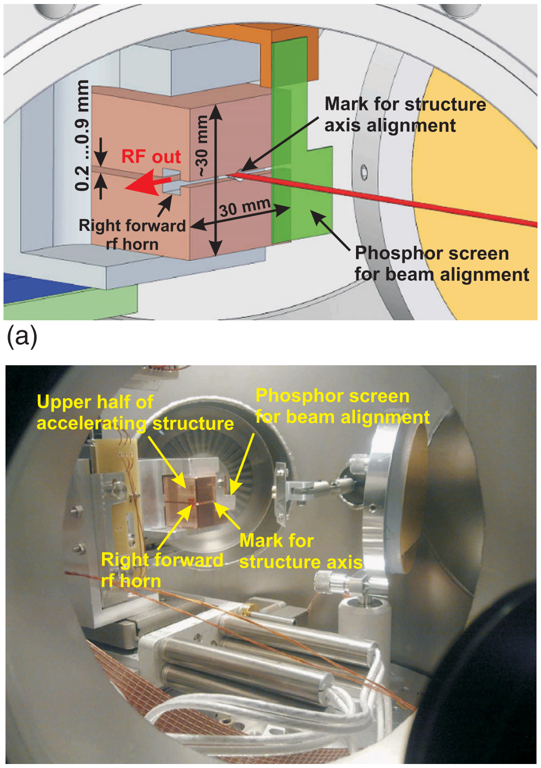

FIG. 17. First experiment: alignment camera view (a), first experiment: Structure and phosphor screen view from the alignment-camera window(b).

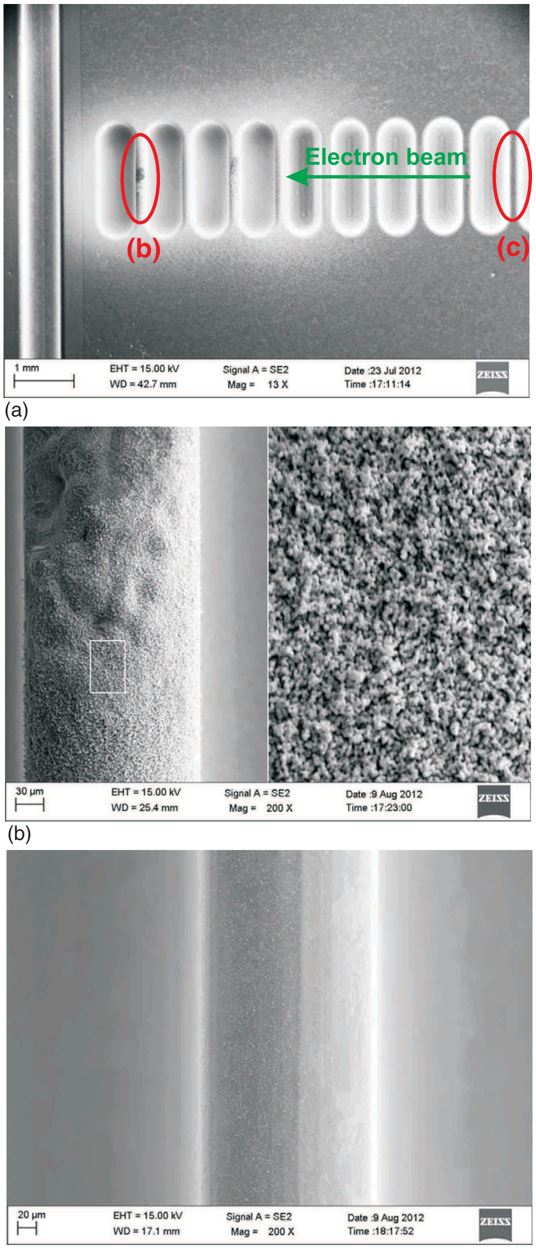

FIG. 18. SEM microscope picture of breakdowns generated during the experiment involving the first copper structure, driven by a bunch charge of 2.7 nC and 50 μm length. Output end of the structure (a), 1st iris breakdown damage (b), 9th iris no breakdown damage (c).

most. This damage pattern is consistent with standing waves formed by the reflections from the coupler. Several irises were damaged and metal dust was found in the surrounding cells. After the 9th cell from the output coupler we did not see any damage. Therefore we can say that the nondamage accelerating gradient is the field present in the part of the structure far from the output coupler, working in the traveling wave regime. It is 0.1 GV/m with a peak surface electric field of 0.35 GV/m and pulse length of 2.45 ns. Near the coupler cells, where we saw damage, the field increases, approximately by a factor of two.

C. Second experiment: TW copper structure

The second experiment involving the copper traveling wave structure, is illustrated in Fig. 19. It was installed in the vacuum chamber with remotely controlled motorized stages to shift the structure horizontally or vertically with respect to the electron beam. There was also a motor to adjust the gap between the two halves of the structure.

The second experiment ran with about 3.2 nC bunch charge. We started the experiment with a gap of 0.9 mm.

We made several horizontal scans, repeating this procedure until the minimum gap of 0.2 mm. When the structure center was aligned with respect to the beam the pyro signal was very stable and its fluctuations were correlated with bunch charge fluctuations, no light from inside the structure was seen by the alignment camera. We did not observe any obvious signatures of rf breakdown on the pyrodetector signal. Rare vacuum bursts happened at the highest power 7.7 MW.

After the experiment, no breakdown damage was present in the input coupler (Fig. 20) when viewed with SEM. The breakdowns occurred after cell number 16, as depicted in

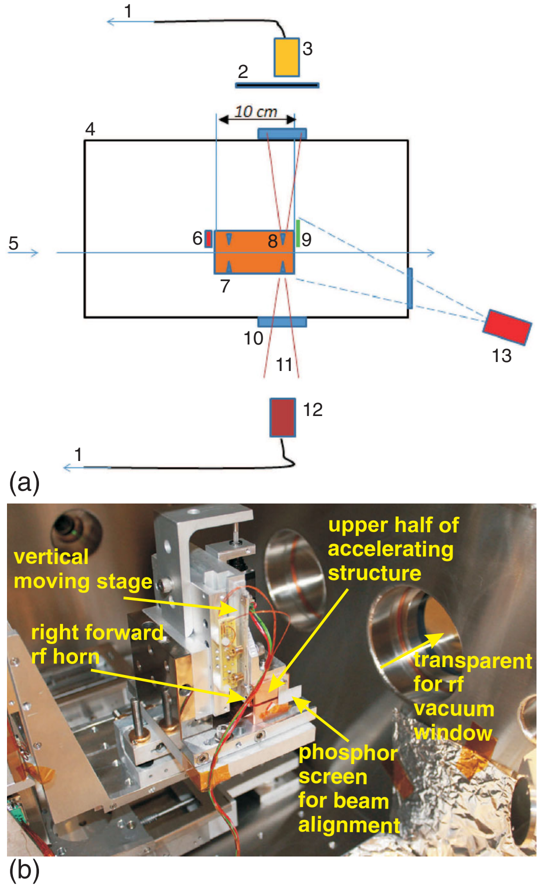

FIG. 19. Second experiment setup (a): signal to scope (1), remotely controlled rf beam shutter (2), crystal detector (3), kraken vacuum chamber (4), electron beam (5), laser alignment mirror (6), right reflected rf horn (7), left forward rf horn (8), phosphor (9), rf window (10), output rf beam (11), pyrodetector (12), video camera for beam-structure alignment and rf breakdown diagnostic (13), picture of the device (b).

Fig. 21. As a result of the SEM autopsy, a massive breakdown damage was discovered after the first 20 cells from the input coupler, while the other cells were undamaged and therefore able to withstand the induced field. We treated the nondamaged cells as one undamaged accelerator. Comparing the experimental results with the numerical calculations it is possible to estimate the field levels at which the structure was not damaged. From the numerical simulations of the fundamental mode with gap 0.2 mm (corresponding to the highest gradient), the peak nondamage surface electric field was 0.64 GV/m and the accelerating gradient was 0.3 GV/m. Considering the sum of all modes, the peak surface electric field was 1.5 GV/m. At this gap the attenuation is very high and the attenuation length is 2.38 ns (Table III). This means that for the wave with the group velocity $v_g = 0.2$ m/s, the signal decays in 2.38 ns.

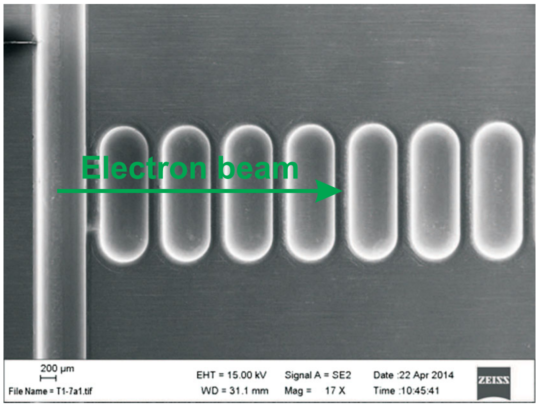

FIG. 20. TW copper input coupler, cells 1–7, no damage.

D. Third experiment: TW stainless steel structure

The third experiment, involving the stainless steel traveling wave structure, is illustrated in Fig. 22. The experiment ran with a bunch charge of about 3 nC and a bunch length of about 50 μm. In the previous experiments we were not able to detect rf breakdowns from the rf signal. In this last experiment we built an arc detector. The two metal halves that compose the structure were electrically insulated from ground and each other using plastic film. This made it possible to measure the field emission current by measuring the current induced in the two separate metal blocks. This was achieved by connecting the two metal halves to an oscilloscope and by measuring the induced current. Signatures of rf breakdown is a spike in the current monitor signal.

The same scan procedure used in the second experiment was repeated for the third, varying the gap from 0.9 to 0.5 mm. The pulse energy of the output signal was measured with a pyrodetector. Two pulse energy measurements are shown in Fig. 23 (gap = 0.7 mm, gap = 0.5 mm), and compared with predicted values. The pyrodetector that measures the pulse energy, also detects the diffraction radiation that is a systematic offset added to the measured signal. Therefore, to compare the measured pulse energy with the calculated one, the diffraction radiation component must be subtracted from the main signal, but we do not have tools to evaluate it precisely. Therefore to compare measurements and simulations we matched the measured and calculated plots using the least-squares method.

The largest output energy that we measured when the beam was on the structure axis is shown in Fig. 24, as a function of the gap.

During the experiment we observed the rf breakdowns with the arc detector. Two examples are shown in Fig. 25. This figure reports the energy measured by the pyrodetector (a),(c), and the arc detector (b),(d). Without rf breakdowns the shape of the signal on the current monitor is similar to the pyrodetector. Figure 25(d) shows how rf breakdowns destroy the shape of the current monitor signal when the gap was reduced from 0.7 to 0.6 mm.

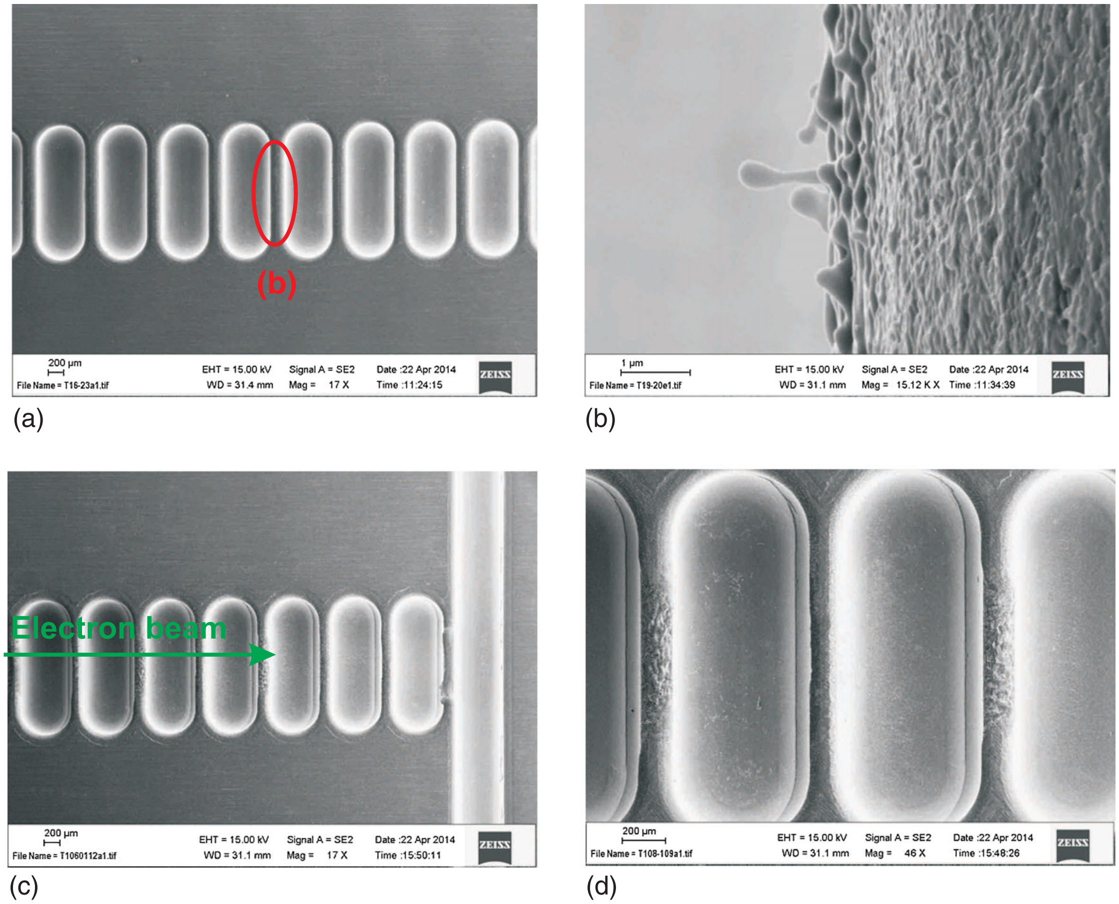

FIG. 21. SEM microscope of the breakdowns generated during the experiment involving the TW copper structure, driven by a bunch of charge of 3.2 nC and 50 μm long. Cells number 16–23, fist signs of damage (a), iris 19–20, fist signs of damage (b), output coupler, massive breakdown damage (c), cells 108–109, breakdown damage (d).

After the experiment, a SEM inspection of the structure was performed and it is shown in Fig. 26. It is possible to see the damages on the metal surface. Figure 26 show that no damage was created in the output coupler or in the irises 110–111. In Fig. 26(h) the damaged areas are on a common line. We concluded that the electron beam touched the structure causing the damage. This beam damage weakened the structural surface, facilitating the generation of rf breakdowns up to even a 0.9 mm gap. Figure 27 compares the recorded arc detector before the beam damage at the beginning of the shift (b) and after the beam damage at the end of the shift (d) with 0.9 mm gap.

The beam damage in the input coupler [Fig. 26(e)] is similar to the pulse heating damage in high gradient rf structures [69]. Figure 26(h) of cells 9–10 show rf breakdown caused by beam damage.

In the surfaces not damaged by the electron beam we did not see rf breakdown damages. This means that the stainless steel surfaces can withstand the induced electric field. At the minimum gap of 0.5 mm, corresponding to the maximum electric field, we can estimate a nondamage accelerating gradient, which is 0.19 GV/m with a peak surface electric field of 1 GV/m and a pulse length of 0.33 ns.

VI. SUMMARY AND DISCUSSION

This paper reports experimental results from a study of the physics of rf breakdown in high gradient copper and stainless steel mm-wave accelerating structures. The FACET ultrarelativistic electron bunch was used to excite electromagnetic fields in the structures. Our ultimate goal was to have the full breakdown statistics at mm-wave frequencies. Since the electron beam was only available for few hours, we limited our studies to find the peak electric field and pulse length at which the structures were not damaged by rf breakdowns. Three types of structures were tested: copper traveling wave operating in standing wave regime, copper traveling wave and stainless steel traveling wave.

The wakefields induced by the electron bunch were estimated by a frequency domain method that uses periodic

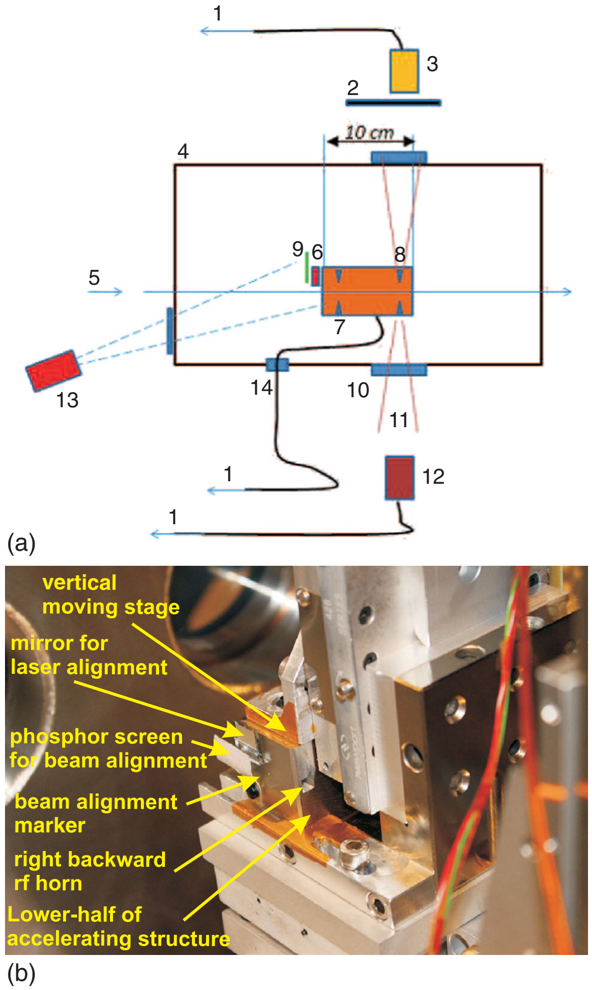

FIG. 22. Third experiment setup (a): signal to scope (1), remotely controlled rf beam shutter (2), crystal detector (3), vacuum chamber (4), electron beam (5), laser alignment mirror (6), right reflected rf horn (7), left forward rf horn (8), phosphor (9), rf window (10), output rf beam (11), pyrodetector (12), video camera for beam-structure alignment and rf breakdown diagnostic (13), vacuum feed-through (14), picture of the device (b).

eigensolutions. Such a method takes into account the wall losses and is applicable to complex cell geometries.

At each test, new diagnostics were developed and we understood more about the behavior of the structures. In the third experiment we developed an arc detector. The two metal halves were electrically insulated. This has been achieved by connecting the two metal halves to an oscilloscope and by measuring the induced current. The arcs were detected by observing the spikes in the signal.

After each experiment the structure was inspected with a SEM autopsy showing the breakdowns generated by the high-induced electric fields.

Here we draw on our experience with high gradient tests of X-band traveling wave accelerating structures.

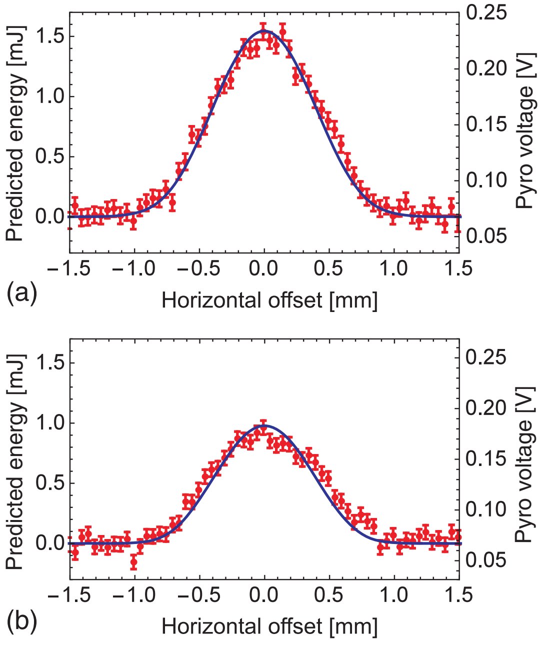

FIG. 23. Predicted (blue) and measured (red) pulse energy in function of the horizontal position of a 3 nC electron beam, for stainless steel structures of gap $= 0.7$ mm (a), gap $= 0.5$ mm (b).

As of now, the most systematic study of rf breakdowns were done at X-band. In the experiments with X-band traveling wave accelerating structures we measure the position of every breakdown and thus we know the breakdown probability in every cell. The structures can have events with multiple breakdowns during single pulse but probability of such events is typically less than 30%. So the majority of breakdowns are single breakdown events, were one breakdown does not induce another one in different part of the structure. Appearance of "hot cells" in some structures is another indication of relative independence on structure parts. "Hot cell" is a

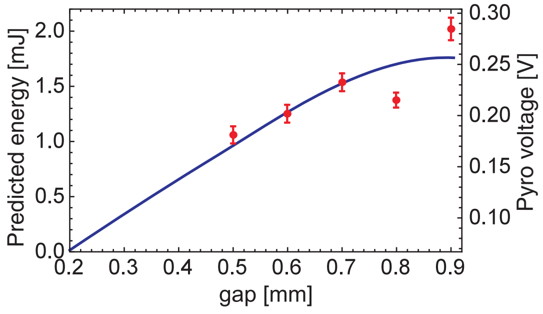

FIG. 24. Predicted (blue) and measured (red) peak pulse energy in function of the gap, for a 3 nC electron beam (Stainless steel structure).

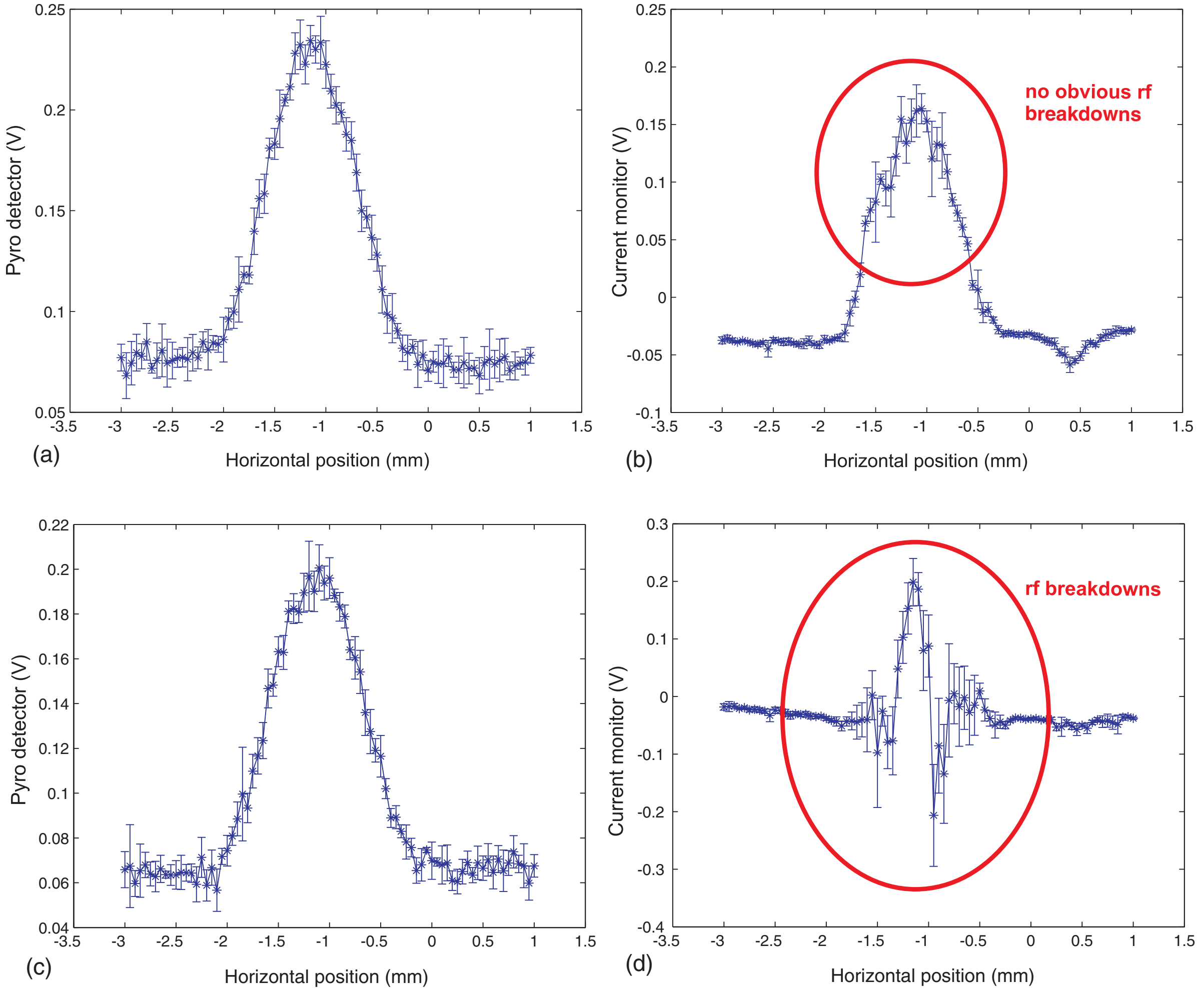

FIG. 25. First observation of rf breakdowns on current monitor, electron beam scan with FACET. Sections (a,b) data: gap = 0.7 mm, q = 3 nC, $E_{z0} = 0.17$ GV/m, $E_{\max} = 0.52$ GV/m, $l_{att}/v_g = 0.35$ ns. Sections (c,d) data: gap = 0.6 mm, q = 3 nC, $E_{z0} = 0.16$ GV/m, $E_{\max} = 0.5$ GV/m, $l_{\mathrm{att}}/v_g = 0.35$ ns.

cell that has breakdown probability higher than neighboring cells. Once appears the "hot cell" stays in same location and does not increase probability of breakdowns in neighboring cells. These X-band experimental data lead us to a conjecture that the breakdowns in upstream part of our 100 GHz traveling wave structure are independent of breakdowns in downstream part. This allows us to imply that "nondamage" condition in upstream part is practically independent from breakdown events in downstream part. Since in all three structures we always found a zone without breakdowns, we used that area as one undamaged accelerator and we concluded that the nondamage conditions are the maximum fields and pulse length induced by the bunch in that specific area. We summarize the nondamage conditions in Table IV.

Statistical properties of rf breakdown which typically has close to Poisson distribution and is characterized by an average probability. This probability is a function of both rf fields and pulse shape. Pulse shape is often reduced to just pulse length (τ_p), or time period for which the metal surface is exposed to rf fields. In X-band structures a typical dependence of the breakdown probability on the pulse length is very strong, τ_p^6 [26,32]. In a traveling wave structure fed by an rf source the pulse length is the same in every cell. So relative cell-to-cell breakdown probability depends on local rf electric, magnetic fields and their combination such as modified Poynting vector. In the experiments described in our paper, our constant impedance structure is excited by an ultrarelativistic charge. Therefore, peak fields are the same in every cell but the effective pulse length is different. The downstream cells are exposed to rf fields longer than upstream cells. If the strong pulse length dependence of the breakdown probability exists in 100 GHz structures then we should see downstream

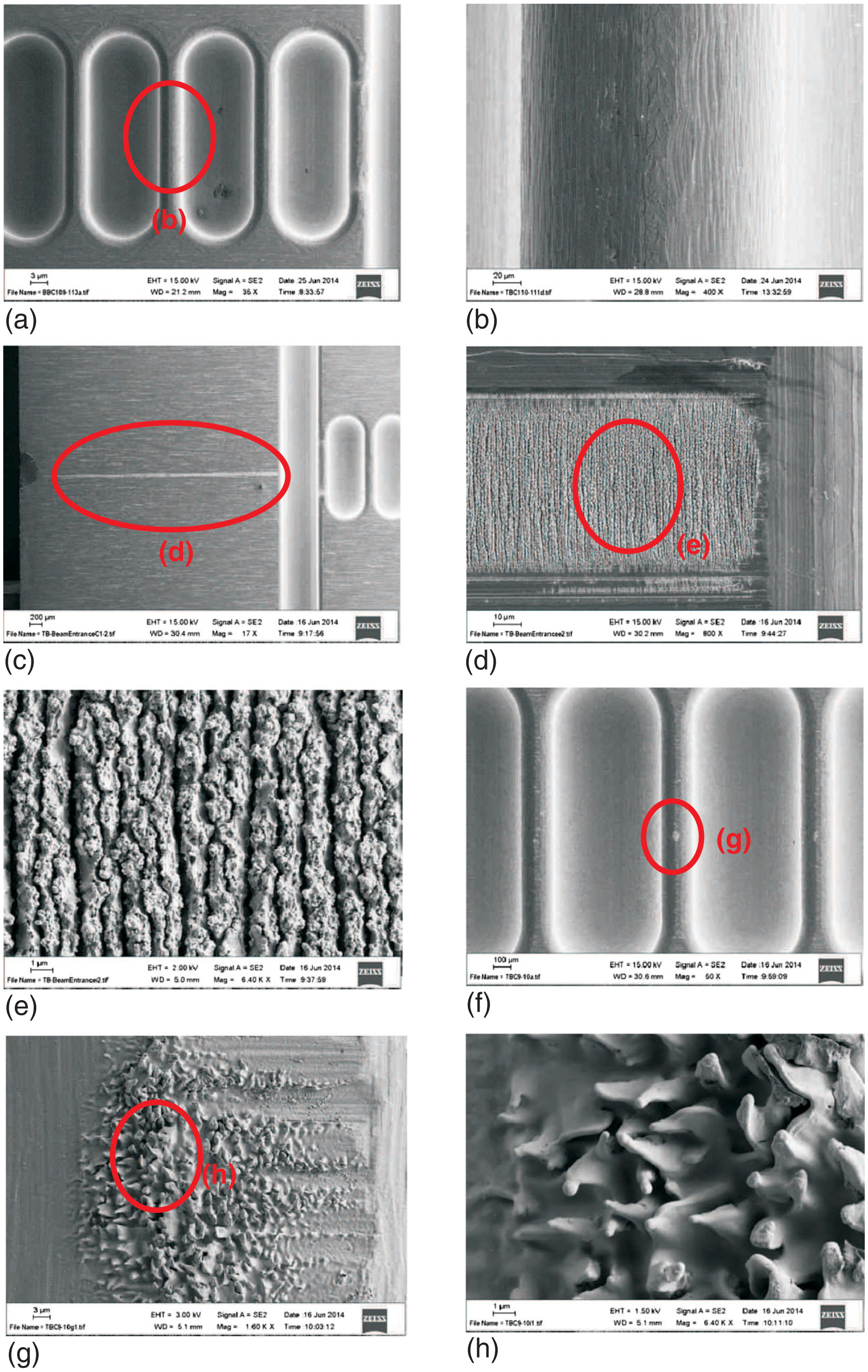

FIG. 26. SEM microscope of the breakdowns generated during the experiment involving the TW stainless steel structure, driven by a bunch of charge of 3 nC and 50 μm long. Output coupler, no damage (a), iris 110–111, no damage (b), input coupler, beam damage, looks similar to pulse heating damage we see in high gradient rf structures (c)–(e), cells 9–10 rf breakdown damage which is aligned with beam damage, rf breakdowns were likely caused by accidental beam damage to few irises (f)–(h).

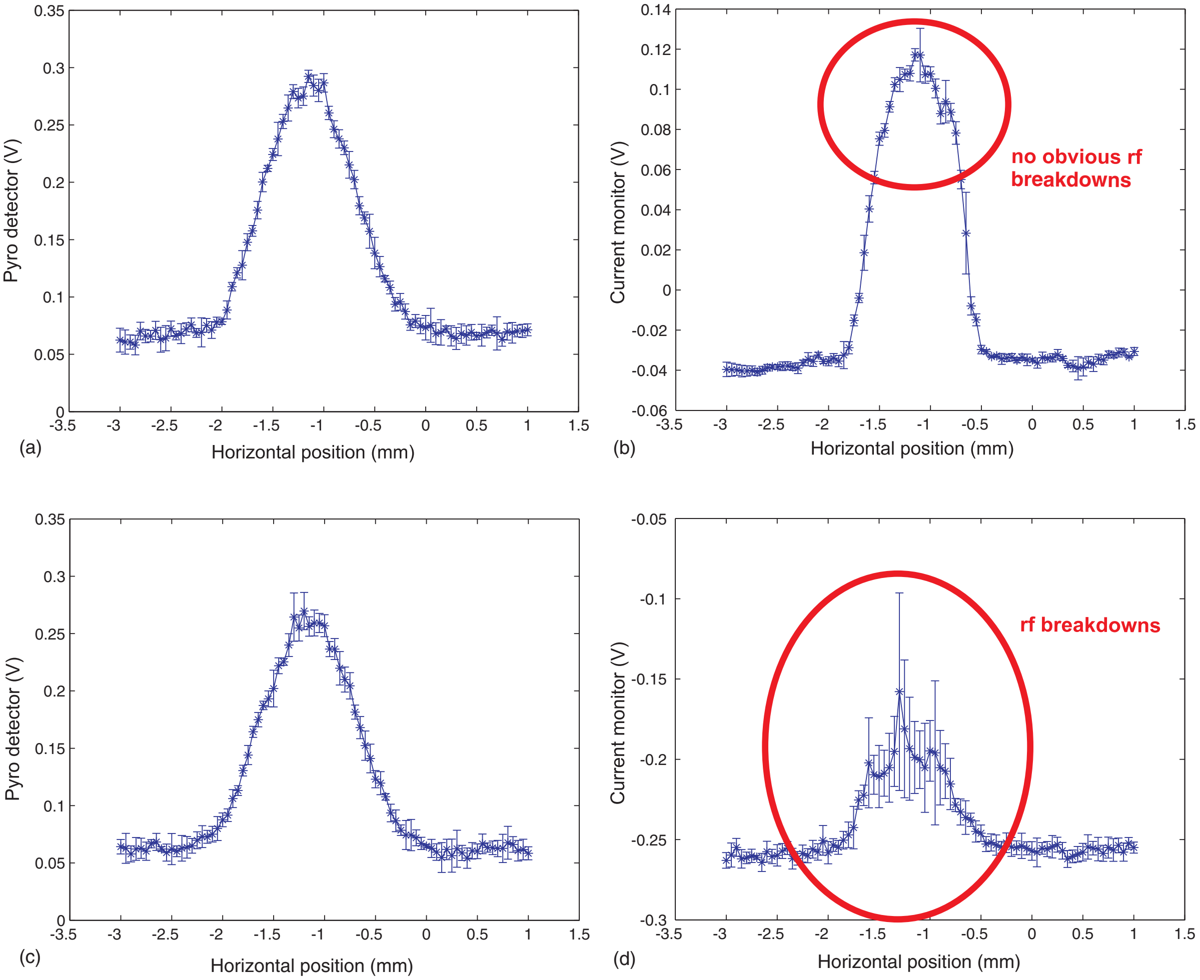

FIG. 27. Irreversible damage, electron beam scan for the same aperture at the beginning of the shift (a,b) and the end of the shift (c,d), with 0.9 mm gap, charge 3 nC.

cells damaged before upstream. This is exactly what we observe in autopsies of our structures.

In these experiments we found high gradients in mm-wave structures and we made rf breakdowns tests at such frequencies. These studies will pave the way toward the use of these devices in future accelerators applications.

TABLE IV. Nondamage conditions, measured in the three experiments: copper wave structure operating in the standing wave regime, traveling wave copper and stainless steel structure.

Parameters	Unit	Cu SW	Cu TW	Steel TW
Min gap ($2a$)	[mm]	0.9	0.2	0.5
Charge (q)	[nC]	2.7	3.2	3
Bunch length (σ_z)	[mm]	0.05	0.05	0.05
E_{acc}	[GV/m]	0.1	0.3	0.19
$E_{\mathrm{max,(fund.mode)}}$	[GV/m]	0.35	0.64	0.52
$E_{\mathrm{max,alltrap.modes}}$	[GV/m]	0.35	1.5	1
l_{att}	[mm]	91	1.5	3.5
t_p	[ns]	2.45	2.38	0.33

ACKNOWLEDGMENTS

Work supported by the U.S. DOE under Contract No. DE-AC02-76SF00515. We thank all the E204 experiment crew: Juan Cruz Jr., RF Diagnostics: Brendan O'Shea, Spencer Gessner, Oliver Williams (UCLA), Filippos Toufexis. SEM: Chris Pearson. Machine optics and other informations: Erik Adli, Carl Andreas Lindstrom, Michael Litos. We especially thank Vitaly Yakimenko and FACET team for excellent support.

[1] R. B. Neal, D. W. Dupen, H. A. Hogg, and G. A. Loew, The Stanford two mile accelerator Report No. SLAC-REPRINT-1968-001.

[2] S. Doebert *et al.*, High gradient performance of NLC/GLC X-band accelerating structures in *Proceedings of the 21st Particle Accelerator Conference, Knoxville, TN, 2005* (IEEE, Piscataway, NJ, 2005), p. 372.

[3] J. W. Wang, R&D of accelerator structures at SLAC, *High Energy Phys. Nucl. Phys.* ***30****, 11 (2006).*

[4] G. Guignard (The CLIC Study Team), The CLIC Study Team, CERN Report No. CERN 2000-008.

[5] F. V. Hartemann and F. Albert, Design of a 2 MeV Compton scattering gamma-ray source for DNDO missions, LLNL Technical Report, LLNL-TR-416320, 2009.

[6] D. H. Whittum, Millimeter-Wave Drivers for Future Linear Colliders in *22nd International Conference on Infrared and Millimeter Waves, Wintergreen, USA, 1998*, Report No. SLAC-PUB-7809, 1998.

[7] G. A. Loew and J. W. Wang, RF Breakdown Studies in Room Temperature Electron Linac Structures, Report No. SLAC-PUB-4647, 1988.

[8] H. H. Braun, S. Döbert, I. Wilson, and W. Wuensch, Frequency and Temperature Dependence of Electrical Breakdown at 21, 30, and 39 GHz, Phys. Rev. Lett. **90**, 224801 (2003).

[9] C. Adolphsen, Normal Conducting rf Structure Test Facilities and Results in *Proceedings of the 2003 Particle Accelerator Conference, Portland, OR* (IEEE, New York, 2003), p. 668.

[10] G. Geschonke, Result from the CLIC Test Facility CTF3 and Update on the CLIC Design in *Proceedings of the 11th European Particle Accelerator Conference, Genoa, 2008* (EPS-AG, Genoa, Italy, 2008), p. 2912.

[11] G. D'Auria, X-band technology applications at FERMI@Elettra FEL project, Nucl. Instrum. Methods Phys. Res., Sect. A **657**, 150 (2011).

[12] J. Beijers *et al.*, ZFEL: A Compact, Soft X-ray FEL in the Netherlands in *Proceedings of the 32nd Free Electron Laser Conference, Malmö, Sweden* (Max-lab, Sweden, 2010), p. 163.

[13] U. Amaldi *et al.*, CYCLINACS: Novel fast-cycling accelerators for hadron therapy, arXiv:0902.3533.

[14] A. E. Vlieks *et al.*, Initial Testing of the Mark-0 X-Band RF Gun at SLAC in *Proceedings of the 3rd International Particle Accelerator Conference, New Orleans, LA, 2012* (IEEE, Piscataway, NJ, 2012).

[15] P. McIntosh *et al.*, Realization of an X-Band RF System for LCLS in *Proceedings of the 21st Particle Accelerator Conference, Knoxville, TN, 2005* (IEEE, Piscataway, NJ, 2005).

[16] V. A. Dolgashev, X-Band Deflectors in *ICFA Beam Dynamics Mini-Workshop on Deflecting/Crabbing Cavity Applications in Accelerators Cockcroft Institute* (CERN, Daresbury, UK, 2010).

[17] V. A. Dolgashev, G. Bowden, Y. Ding, P. Emma, P. Krejcik, J. Lewandowski, C. Limborg, M. Litos, J. Wang, and D. Xiang, Design and application of multimegawatt X-band deflectors for femtosecond electron beam diagnostics, Phys. Rev. ST Accel. Beams **17**, 102801 (2014).

[18] S. G. Tantawi and others, Application of the Balanced Hybrid Mode in Overmoded Corrugated Waveguides to Short Wavelength Dynamic Undulators in *Proceedings of the 2nd International Particle Accelerator Conference, San Sebastián, Spain* (EPS-AG, Spain, 2011).

[19] S. Tantawi, M. Shumail, J. Neilson, G. Bowden, C. Chang, E. Hemsing, and M. Dunning, Experimental Demonstration of a Tunable Microwave Undulator, Phys. Rev. Lett. **112**, 164802 (2014).

[20] V. A. Dolgashev, Progress on high-gradient structures, AIP Conf. Proc. **1507**, 76 (2012).

[21] J. Wang *et al.*, Fabrication Technologies of the High Gradient Accelerator Structures at 100 MV/m Range in *Proceedings of the International Particle Accelerator Conference, Kyoto, Japan* (ICR, Kyoto, 2010).

[22] T. Higo *et al.*, Advances in X-band TW Accelerator Structures Operating in the 100 MV/m Regime in *Proceedings of the International Particle Accelerator Conference, Kyoto, Japan* (ICR, Kyoto, 2010), p. 3702.

[23] T. Higo, Progress of X-band Accelerating Structures in *Proceedings of the 25th International Linear Accelerator Conference, LINAC-2010, Tsukuba, Japan* (KEK, Tsukuba, Japan, 2010).

[24] W. Wuensch, Status and objectives of the CLIC X-band activity in *International Workshop on Breakdown Science and High Gradient Technology in Tsukuba, Japan* (CERN, Tsukuba, 2012).

[25] V. Dolgashev, High gradient results from single-cell setup in *International Workshop on Breakdown Science and High Gradient Technology in Tsukuba, Japan* (CERN, Tsukuba, 2012).

[26] V. Dolgashev, S. Tantawi, Y. Higashi, and B. Spataro, Geometric dependence of radio-frequency breakdown in normal conducting accelerating structures, Appl. Phys. Lett. **97**, 171501 (2010).

[27] F. Wang, C. Adolphsen, and C. Nantista, Performance limiting effects in X-band accelerators, Phys. Rev. ST Accel. Beams **14**, 010401 (2011).

[28] V. A. Dolgashev and S. G. Tantawi, Simulations of Currents in X-band accelerator structures using 2D and 3D particle-in-cell code in *Proceedings of the Particle Accelerator Conference, Chicago, IL, 2001* (IEEE, New York, 2001), p. 3807.

[29] V. Dolgashev and S. Tantawi, Effect of rf parameters on breakdown limits in high-vacuum X-band structures, AIP Conf. Proc. **691**, 151 (2003).

[30] V. A. Dolgashev, High magnetic fields in couplers of X-band accelerating structures in *Proceedings of the 2003 Particle Accelerator Conference, Portland, OR* (IEEE, New York, 2003), p. 1267.

[31] V. A. Dolgashev and S. G. Tantawi, RF Breakdown in X-band Waveguides in *Proceedings of the 8th European Particle Accelerator Conference, Paris, 2002* (EPS-IGA and CERN, Geneva, 2002), p. 2139.

[32] A. Grudiev, S. Calatroni, and W. Wuensch, New local field quantity describing the high gradient limit of accelerating structures, Phys. Rev. ST Accel. Beams **12**, 102001 (2009).

[33] D. Whittum, H. Henke, and P. Chou, High-gradient cavity beat-wave accelerator at W-band in *Proceedings of the Particle Accelerator Conference, Vancouver, BC, Canada, 1997* (IEEE, New York, 1997), p. 542.

[34] A. W. Chao and M. Tigner, Handbook of Accelerator Physics and Engineering, *Handbook of Accelerator Physics and Engineering* (World Scientific, Singapore, 1999).

[35] D. H. Whittum and S. G. Tantawi, Switched matrix accelerator, Rev. Sci. Instrum. **72**, 73 (2001).

[36] D. H. Whittum and S. G. Tantawi, Active millimeter wave accelerator with parallel beams, Report No. SLAC-PUB-7845.

[37] SLAC W-band program, http://www.slac.stanford.edu/grp/arb/tn/histpap/wband/.

[38] M. E. Hill, C. Adolphsen, W. Baumgartner, R. S. Callin, X. E. Lin, M. Seidel, T. Slaton, and D. H. Whittum, High-Gradient Millimeter-Wave Accelerator on a Planar Dielectric Substrate, Phys. Rev. Lett. **87**, 094801 (2001).

[39] M. Hill, W. Fowkes, X. Lin, and D. Whittum, Beam-cavity interaction circuit at W-band, IEEE Trans. Microwave Theory Tech. **49**, 998 (2001).

[40] M. Hill, R. Callin, M. Seidel, and D. Whittum, High-power squeeze-type phase shifter at W-band, IEEE Trans. Microwave Theory Tech. **50**, 1437 (2002).

[41] M. Hill, R. Callin, and D. H. Whittum, High-power vacuum window in WR10, IEEE Trans. Microwave Theory Tech. **49**, 994 (2001).

[42] F. Zimmermann, D. H. Whittum, C. K. Ng, and M. E. Hill, Wake fields in a mm-wave linac, AIP Conf. Proc. **472**, 270 (1999).

[43] H. Henke, Planar structures for electron acceleration in *Proceedings of the Particle Accelerator Conference, Dallas, TX, 1995* (IEEE, New York, 1995), p. 1750.

[44] B. Littmann and H. Henke, Feasibility study of optically coupling RF-power at mm waves in *Proceedings of the Particle Accelerator Conference, Dallas, TX, 1995* (IEEE, New York, 1995), p. 1593.

[45] W. Bruns, Design of input couplers and endcells for side coupled muffin-tin structures in *Proceedings of the Particle Accelerator Conference, Dallas, TX, 1995* (IEEE, New York, 1995), p. 1088.

[46] W. Bruns, Error sensitivity study for side coupled muffin tin structures using a finite difference program in *Proceedings of the Particle Accelerator Conference, Dallas, TX, 1995* (IEEE, New York, 1995), p. 1085.

[47] P. Chou, G. Bowden, M. Copeland, H. Henke, A. Menegat, and R. Siemann, Design and fabrication of a traveling-wave muffin-tin accelerating structure at 90 GHz in *Proceedings of the Particle Accelerator Conference, Vancouver, BC, Canada, 1997* (IEEE, New York, 1997), p. 464.

[48] P. J. Chou, G. B. Bowden, M. R. Copeland, A. Farvid, R. E. Kirby, A. Menegat, C. Pearson, L. Shere, R. H. Siemann, J. E. Spencer, and D. H. Whittum, The fabrication of millimeter-wavelength accelerating structures, AIP Conf. Proc. **398**, 501 (1997).

[49] P. Chou, G. Bowden, M. Copeland, H. Henke, A. Menegat, D. Pritzkau, and R. Siemann, RF measurements of a traveling wave muffin-tin accelerating structure at 90 GHz in *Proceedings of the Particle Accelerator Conference, Vancouver, BC, Canada, 1997* (IEEE, New York, 1997), p. 672.

[50] N. Kroll, E. Hill, X. Lin, R. Siemann, D. Vier, D. Whittum, and D. Palmer, Planar accelerator structures for millimeter wavelengths in *Proceedings of the 18th Particle Accelerator Conference, New York, 1999* (IEEE, New York, 1999), p. 3612.

[51] Facility for advanced accelerator experimental tests (FACET), http://facet.slac.stanford.edu/.

[52] G. Andonian, D. Stratakis, M. Babzien, S. Barber, M. Fedurin, E. Hemsing, K. Kusche, P. Muggli, B. O'Shea, X. Wei, O. Williams, V. Yakimenko, and J. B. Rosenzweig, Dielectric Wakefield Acceleration of a Relativistic Electron Beam in a Slab-Symmetric Dielectric Lined Waveguide, Phys. Rev. Lett. **108**, 244801 (2012).

[53] M. C. Thompson, H. Badakov, J. B. Rosenzweig, G. Travish, M. Hogan, R. Ischebeck, N. Kirby, R. Siemann, D. Walz, P. Muggli *et al.*, Ultra-High Gradient Dielectric Wakefield Accelerator Experiments, 2006, http://www.osti.gov/scitech/servlets/purl/894768.

[54] M. C. Thompson, H. Badakov, A. M. Cook, J. B. Rosenzweig, R. Tikhoplav, G. Travish, I. Blumenfeld, M. J. Hogan, R. Ischebeck, N. Kirby, R. Siemann, D. Walz, P. Muggli, A. Scott, and R. B. Yoder, Breakdown Limits on Gigavolt-per-Meter Electron-Beam-Driven Wakefields in Dielectric Structures, Phys. Rev. Lett. **100**, 214801 (2008).

[55] J. B. Rosenzweig, G. Andonian, P. Muggli, P. Niknejadi, G. Travish, O. Williams, K. Xuan, and V. Yakimenko, High Frequency, High Gradient Dielectric Wakefield Acceleration Experiments at SLAC and BNL, AIP Conf. Proc. **1299**, 364 (2010).

[56] High frequency structural simulator (HFSS), http://www.ansys.com/Products/.

[57] Makino (Elgin, IL, USA), http://www.makino.com/.

[58] Edm department inc. (Bartlett, IL, USA), http://www.edmdept.com/.

[59] C. Nantista, S. Tantawi, and V. A. Dolgashev, Low-field accelerator structure couplers and design techniques, Phys. Rev. ST Accel. Beams **7**, 072001 (2004).

[60] M. Dal Forno, P. Craievich, G. Penco, and R. Vescovo, Theoretical and experimental analysis of a linear accelerator endowed with single feed coupler with movable short-circuit, Rev. Sci. Instrum. **84**, 114701 (2013).

[61] Wolfram mathematica (Champaign, IL, USA), http://www.wolfram.com/mathematica/.

[62] A. Smirnov, Group velocity effect on resonant, long-range wake-fields in slow wave structures, Nucl. Instrum. Methods Phys. Res., Sect. A **480**, 387 (2002).

[63] K. L. F. Bane and G. Stupakov, Impedance of a rectangular beam tube with small corrugations, Phys. Rev. ST Accel. Beams **6**, 024401 (2003).

[64] A. Millich and L. Thorndahl, Loss factor dependence on group velocity in disk-loaded travelling-wave structures, Report No. CERN-CLIC-NOTE-366, 1999.

[65] A. Novokhatsky, The Computer Code NOVO for the Calculation of Wake Potentials of the Very Short Ultra-relativistic Bunches, Report No. SLAC-PUB-11556, 2005.

[66] A. Novokhatski, Field dynamics of coherent synchrotron radiation using a direct numerical solution of Maxwell's equations, Phys. Rev. ST Accel. Beams **14**, 060707 (2011).

[67] A. Novokhatsky, Modeling of Coherent Synchrotron Radiation using a Direct Numerical Solution of Maxwell's Equations, Report No. SLAC-PUB-15258, 2012.

[68] V. Balakin, Beam Dynamics Of A Colliding Linear Electron - Positron Beam (VLEPP), Report No. SLAC-TRANS-0188, 1978.

[69] L. Laurent, S. Tantawi, V. Dolgashev, C. Nantista, Y. Higashi, M. Aicheler, S. Heikkinen, and W. Wuensch, Experimental study of rf pulsed heating, Phys. Rev. ST Accel. Beams **14**, 041001 (2011).